RSC Advances

PAPER

View Article Online
View Journal | View Issue

Cite this: *RSC Adv.*, 2026, **16**, 7410

DFT study of atmospheric characteristics of CF_3SO_2F: the fungibility of the insulation gas of SF_6

Wei Liu,[a] Yuanyuan Zheng,[b] Yuanyuan Cui,[b] Dan Li,[b] Qinqin Yuan,[b] Kun Wang*[b] and Longjiu Cheng *[b]

Received 19th June 2025
Accepted 16th January 2026

DOI: 10.1039/d5ra04357c

rsc.li/rsc-advances

Due to the significant greenhouse effect of SF_6, CF_3SO_2F has emerged as a potential alternative that meets the requirements for insulation gases in high-voltage electrical equipment. Herein, the atmospheric lifetime and global warming potential (GWP) of CF_3SO_2F were evaluated based on its interactions with hydroxide radicals (·OH) using theoretical calculations. By employing the Monte Carlo method, we constructed molecular structures of SF_6–H_2O and CF_3SO_2F–H_2O as mixed-gas systems to simulate the dissociation of these insulation gases under atmospheric conditions. The adversative efficiency (RE) of CF_3SO_2F was determined to be 0.177 W $(m^2\ ppbv)^{-1}$, with an atmospheric lifetime of 52.02 years and a GWP of 4320. The reactive models, developed using density functional theory (DFT) and Car–Parrinello molecular dynamics (CPMD), not only enable the determination of the dissociation pathway in the atmosphere, but also provide detailed insights into the interactions with ·OH based on the overall dynamic behaviour.

1. Introduction

SF_6 plays an essential role in the power industry due to its excellent dielectric strength, heat transfer capability, and arc-quenching ability.[1] Toxic decomposition products can be formed from SF_6 under electric arc conditions, despite the gas itself being non-toxic.[2] SF_6 is a potent greenhouse gas with a 100 year global warming potential (GWP100) of 23 500, equivalent to 23 500 kg CO_2 per kg of SF_6, and an atmospheric lifetime of approximately 3200 years.[3] Global emissions of SF_6 have been increasing, reaching 9040 tons in 2018, with the power industry accounting for 80% of this total. Consequently, atmospheric concentrations of SF_6 have risen from 0.66 parts per trillion (ppt) by volume in 1978 to over 11 ppt in 2022.[4,5] Faced with this rapid accumulation and its permanent climate impact, aggressively implementing mitigation strategies and switching to sustainable alternatives is an urgent priority. Over the past decades, great efforts have been devoted to identifying such replacements, and several potential alternatives were reported, including $C_5F_{10}O$ and C_3F_7CN.[6,7] However, these gases often suffer from drawbacks, such as high liquefaction temperatures and potential toxicity. Furthermore, despite having potentially superior dielectric strength and lower GWP values than SF_6, their GWP values are still relatively high, limiting their applicability as environmentally friendly insulation media.[8,9]

CF_3SO_2F has attracted considerable attention as a promising replacement for SF_6 due to its excellent insulation performance, low boiling point of −22 °C, and low GWP value.[10–15] Studies of field-dependent electron–molecule capture rates suggest that CF_3SO_2F possesses a higher dielectric strength than SF_6.[9] Both theoretical and experimental investigations have confirmed that the thermal stability of CF_3SO_2F is comparable to that of SF_6.[15] Furthermore, CF_3SO_2F has been demonstrated to exhibit a short atmospheric lifetime and a minimal contribution to smog formation,[16] along with a higher breakdown voltage (32 kV) than that of SF_6 (26 kV).[17] These properties collectively suggest that it is more environmentally friendly and suitable for replacing SF_6 in electrical equipment. Although its boiling point is higher than that of SF_6 (−63.8 °C), its strong dielectric strength and high thermal stability make it applicable in most geographical regions.[12] Zhang *et al.* reported that CF_3SO_2F mainly decomposes *via* C–S bond cleavage, yielding CF_3 and SO_2F radicals. These radicals can further react with free F radicals to form CF_4 and SO_2. Alternatively, decomposition can proceed through CF_3 migration and memorization, forming the more stable intermediate CF_3OSFO, which subsequently decomposes into CF_2O and SOF_2.[18] Wang's team has conducted an in-depth analysis of CF_3SO_2F decomposition products.[19]

The atmospheric behavior and ultimate fate of an insulation gas are directly determined by its reactivity under atmospheric conditions. The most reliable method for estimating the lifetime of a trace gas involves chemical transport models (CTMs), which require accurate rate constants for reactions with ·OH as critical input parameters.[13] For chemically reactive trace gases, atmospheric degradation by ·OH is often the dominant process governing their global atmospheric lifetime. Therefore, to

[a]*State Grid Anhui Electric Power Co., Ltd., Electric Power Research Institute, Anhui, 230601, China*

[b]*Department of Chemistry, Key Laboratory of Functional Inorganic Materials of Anhui Province, Anhui University, Hefei, Anhui, 230601, P. R. China. E-mail: wangkun@ahu.edu.cn; clj@ustc.edu*

evaluate the environmental impact of the insulation gas SF_6 and its alternatives, it is essential to establish a systematic model that simulates atmospheric dissociation based on structure–property relationships. Constructing such mixed-gas models is necessary to fully elucidate the atmospheric interaction mechanisms between insulation gases and ·OH.

In this work, we first compared the electronic structures and RE of SF_6 and CF_3SO_2F based on their optimized molecular geometries. Given that ·OH plays a key role as a reactive species interacting with greenhouse gases in the atmosphere, a co-crystal structure of CF_3SO_2F and H_2O with a 1 : 1 molar ratio was constructed using the MC method. The complete set of four dissociation pathways of CF_3SO_2F with ·OH in the atmosphere was revealed through Car–Parrinello molecular dynamics (CPMD) simulations. Based on the analysis of the reaction pathways, reaction rates, atmospheric lifetime, and GWP were calculated. The combined computational framework of density functional theory (DFT) and CPMD established in this study provides a reliable basis for systematically evaluating the atmospheric behavior of these gases and screening potential alternatives to SF_6.

2. Computational details

To confirm the computational method, bond lengths of the optimized CF_3SO_2F under several DFT methods were compared with CCSD(T). Benchmark calculations show that the bond lengths values of C–F, C–S, S=O and S–F at the M062X/def2tzvp[20,21] level of theory are the closest to those at the CCSD(T)/aug-cc-pVTZ method. Hence, geometric and electronic structures of SF_6, CF_3SO_2F and H_2O were investigated at the M062X/def2tzvp level of theory, using the Gaussian 16 package.[22] The original and optimized coordinates of the initial structures of SF_6, CF_3SO_2F and H_2O are presented in Tables S1 and S2, respectively.The Wiberg bond indices (WBI), atomic charges, electrostatic potentials, and polarizabilities were obtained in Multiwfn (Table 1).[23]

To obtain the reasonable interaction pathways for the dissociation of SF_6 and CF_3SO_2F with hydroxyl radial in atmosphere. We constructed the crystal (SF_6, SF_6–H_2O, CF_3SO_2F, and CF_3SO_2F–H_2O) using the Monte Carlo (MC) method in Materials Studio (MS) software.[24] Prior to prediction, the Universal Force Field (UFF)[25,26] in the Forcite module was applied to assign force field parameters (Fig. S1). Subsequently, the Polymorph module[27] was used to predict the periodic crystal structures of the molecules (Fig. S2). And the optimized coordinates of the crystal structures of SF_6, SF_6–H_2O, CF_3SO_2F, and CF_3SO_2F–H_2O are presented in Table S3.

Table 1 Comparison of the selected bond distances (Å) of CF_3SO_2F with different theoretical levels

	C–F	C–S	S=O	S–F
B3LYP/def2tzvp	1.33	1.87	1.42	1.57
BP86/def2tzvp	1.33	1.87	1.42	1.57
WB97XD/def2tzvp	1.32	1.86	1.41	1.55
M06-2X/def2tzvp	1.32	1.84	1.41	1.55
MP2/aug-cc-pVTZ	1.32	1.85	1.43	1.58
CCSD(T)/aug-cc-pVTZ	1.32	1.85	1.41	1.55

According to Berskey's theory,[28] 88.6% of organic molecular crystal structures belong to the space groups $P_{21/c}$, P_{212121}, P_1, P_{21}, and $C_{2/c}$ in Table S4. The final structures with the lowest total energies are chosen among the five different space groups. And the final coordinates of the lowest-energy structures of SF_6, SF_6–H_2O, CF_3SO_2F, and CF_3SO_2F–H_2O are presented in Table S5. Based on these lowest-energy structures, the predicted crystal structures of SF_6, SF_6–H_2O, CF_3SO_2F, and CF_3SO_2F–H_2O were further optimized using the CASTEP module[29] in MS with the GGA-PBE functional.[30] Ultrasoft pseudopotentials were used to describe the valence states of elements.[31] Convergence tests for the plane-wave cutoff energy and k-points were performed. The cutoff energies for SF_6, SF_6–H_2O, CF_3SO_2F, and CF_3SO_2F–H_2O were set to 300, 400, 500, and 600 eV, respectively. The Brillouin zones[32] were sampled using k-point grids of $2 \times 1 \times 2$, $1 \times 1 \times 1$, $3 \times 1 \times 1$, and $1 \times 3 \times 5$, respectively. All the test results are summarized in Table S6.

Based on the optimized crystal structures, CPMD simulations were performed. We first carried out the convergence of the wave function and the structural optimization under the NVT ensemble,[33] ensuring that the ion temperature, the virtual kinetic energy of electrons, and the total electronic energy were all converged (Fig. S3). Subsequently, the four systems were directly heated to 2500 K and maintained at this temperature for 5 ps to allow the system to reach equilibrium. Then the temperature has been continuously increased to 3000 K for another 21 ps. The final temperature is converged at 3000 K. The total length of 26 ps (260 000 steps) is enough for obtaining the interaction pathways.[34,35]

Finally, the active energies in the typical four dissociation pathways are obtained based on the CPMD trajectories. k_{OH}[36] is the rate constant of reaction between the greenhouse gas and ·OH, which has been obtained by eqn (1)

$$k_{OH}/\text{mol cm}^{-3}\ \text{s}^{-1} = \frac{k_B T}{h}\left(c^{\Theta}\right)^{-1} \exp\left(-\frac{\Delta_r{}^{\neq} G^{\Theta}}{RT}\right) \quad (1)$$

The reaction energy barrier was computed as the energy difference between the transition state and reactant energies, while the Gibbs free energy change ($\Delta_r G_m{}^{\neq}$) was calculated from the energy difference between products and reactants. c^{Θ} as a standard concentration of 1.0 mol cm^{-3}. The atmospheric lifetime of CF_3SO_2F was estimated based on the group contribution method.[37,38] Then the atmosphere lifetime (τ) is obtained based on eqn (2),

$$\tau = \frac{\alpha}{k_{OH} \cdot c_{OH}} \quad (2)$$

In eqn (2), α is the experienced constant equaling to 2.1 and c_{OH} is the concentration of ·OH in the atmosphere, which is 1×10^6 mol cm^{-3}.[39]

3. Results and discussion

3.1 The electronic structures of gas phase

The optimized structures along with the corresponding charge distribution maps are summarized in Fig. 1. SF_6 is the most common insulation gas (Fig. 1a) used in high-voltage

equipment. SF_6 adopts equivalent sp^3d^2 hybridization to bond with six fluorine atoms, resulting in an S–F bond length of 1.59 Å. The candidate insulation gas CF_3SO_2F (Fig. 1b) has a highly polarized S=O bond, whose bond dissociation energy (BDE) of 163.91 kcal mol^{-1} exceeds that of the S–F bond in SF_6 (110.23 kcal mol^{-1}). The S–C bond in CF_3SO_2F has the lowest BDE, making it the weakest bond and the most probable initial site for bond cleavage during dissociation. As shown in Fig. 1c and d, the electrostatic potential (ESP) values are labeled. SF_6, as a highly symmetrical molecule, exhibits a relatively uniform electrostatic potential distribution with minimal variation. In contrast, CF_3SO_2F has a larger electrostatic potential gradient. A uniform electrostatic potential distribution and a low electrostatic potential gradient contribute to improved insulation performance. Therefore, CF_3SO_2F may be slightly inferior in terms of insulation performance due to its significant variation in electrostatic potential.

As the insulation gas, the most important factor is the molecular stability in the arc extinction, which is determined by the electronic structural properties. In this paper, the stability is evaluated through multiple aspects, including bond dissociation energy, HOMO–LUMO gap, and vertical ionization energy.[40–42] The electronic structure properties of SF_6 and CF_3SO_2F are presented in Table 2. The HOMO–LUMO gap of SF_6 is 15.24 eV. Its VIE and EA are 367.76 kcal mol^{-1} and 1.67 eV, respectively. These values indicate the high stability of SF_6 in high-voltage electric fields regarding its ability to accept and donate electrons. CF_3SO_2F has a molecular volume of 104.74 $Å^3$, which is larger than that of SF_6 (87.53 $Å^3$). A larger molecular size is an effective factor in improving electron absorption efficiency. In CF_3SO_2F, the S=O bond is the most polarized, with a WBI of 2.51. This bond is more stable than the S–F bond in SF_6, which has a WBI of 0.72. The VIE and EA of CF_3SO_2F are 310.64 kcal mol^{-1} and 2.33 eV, respectively. Compared with SF_6, CF_3SO_2F exhibits stronger electron affinity and a larger molecular dipole moment, making it an outstanding insulation gas in the arc extinction process, despite having a lower VIE.

Table 2 The molecular volume (V $Å^{-3}$), HOMO–LUMO gap (E_{H-L} eV^{-1}), vertical ionization energy (VIE, kcal mol^{-1}), electronic affinity (EA eV^{-1}), dipole moment (DM/D), electrostatic potential (ESP, kcal mol^{-1}) and Wiberg bond index (WBI) of typical bonds of the two gas structures

Gas	V	E_{H-L}	VIE	EA	DM	WBI
SF_6	87.53	15.24	367.76	1.67	0	S–F: 0.72
CF_3SO_2F	104.74	13.4	310.64	2.33	1.46	S=O: 2.51; S–F: 1.54 S–C: 0.92; C–F: 1.85

3.2 The RE of insulation gases

RE is a physical quantity used to measure the extent of the impact of changes in the concentration of gases in the atmosphere on radiative forcing, and its variations can directly affect the magnitude of radiative forcing.[38] The radiative forcing (RF) resulting from variations in greenhouse gas concentrations is a crucial concept in climate science, which indicates the magnitude and signs of the drivers of climate change.[43] RE can be accurately predicted through the formula (3) provided by Shine and Myhre,[44]

$$\mathrm{RE} = \sum_i F_i \sigma_i \Delta v \quad (3)$$

F_i represents the spectrally resolved RF per unit cross-section W m^{-2} cm $(cm^2-molecule^{-1})^{-1}$ within a given waveband. This data is derived from the instantaneous RF values calculated by

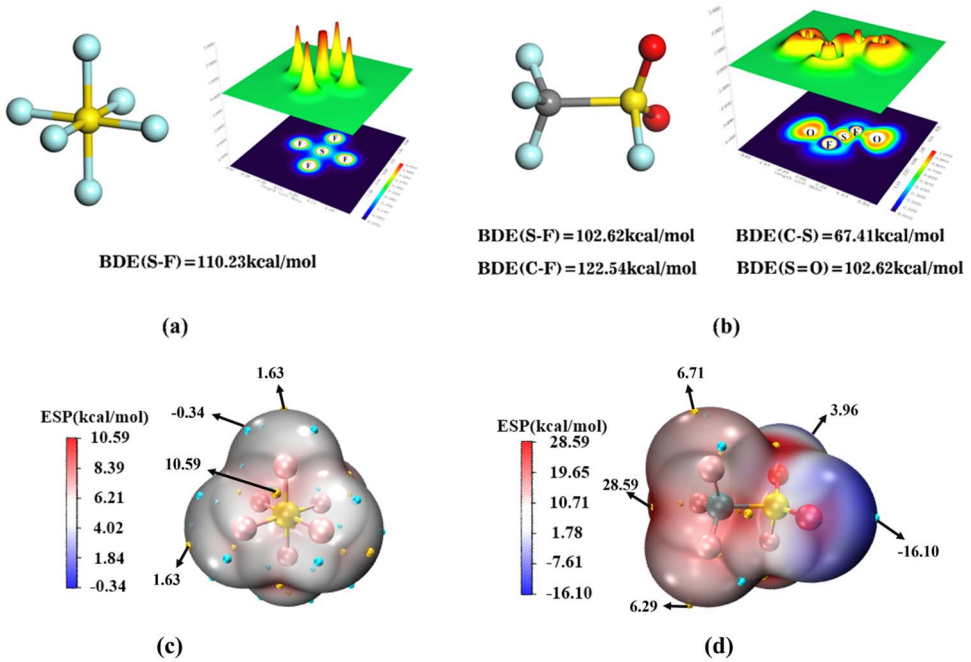

Fig. 1 The optimized gas structures of (a) SF_6 and (b) CF_3SO_2F with the bond dissociation energies (BDE) and charge distribution (blue → red: negative → positive district). Grey: C; green: F; red: O; yellow: S. The electrostatic potential diagrams of SF_6 (c) and CF_3SO_2F (d).

Pinnock *et al.*.[45] Using a narrow-band (10 cm^{-1}) radiative transfer model (NBM) in units of W m^{-2} ppb^{-1}, with the values already accounting for the effects of stratospheric temperature adjustment (STA). We obtained the Raman and infrared intensities of the target gas through theoretical calculations in Fig. 2, using potential energy distribution (PED) analysis,[46] the characteristic vibrational peaks were assigned as follows: for CF_3SO_2F, the asymmetric S=O stretching vibration appeared in the range of 1460–1360 cm^{-1}, CF_3 symmetric bending vibration at 780–760 cm^{-1}, and S–F stretching vibration at 880–850 cm^{-1}; for SF_6, the symmetric F–S–F stretching vibration was observed at 810–790 cm^{-1}, with degenerate bending vibrations at 640–620 cm^{-1}. Then we selected the Raman wavenumber corresponding to the infrared intensity value (data shown in Table 3), and retrieved the corresponding F_i value from the data calculated by Pinnock *et al.* σ_i is the high-resolution absorption cross-section data of the target gas in the band (500–3000 cm^{-1}), with a value of 0.015 cm^2−molecule^{-1} obtained from the HITRAN database. This value has been calibrated using $\nu_{scale} = 29.4 + 0.9475V_{cal}$. where V_{cal} is the theoretical value obtained from DFT calculations and V_{scal} represents the final calibrated value used for GWP estimation. For $\Delta\upsilon$, by combining the instantaneous radiative forcing (IRF) calculated using the high-resolution line-by-line model (OLBL IRF) and the STA adjustment factor (RF/IRF ratio) calculated by the narrow-band model (NBM), we obtained $\Delta\upsilon$ equals to 1 cm^{-1}.[47,48] Compared with the RE of SF_6,[49] which is 0.57 W (m^2 ppbv)$^{-1}$, CF_3SO_2F has an RE value of 0.177 W (m^2 ppbv)$^{-1}$, indicating significantly lower RE.

3.3 Optimized structures in simulated atmospheric environments

A crucial factor for the continuous dissociation of insulation gas is the interactions between insulation gas and ·OH.[50] Since H_2O is the source of ·OH in the atmospheric environment, both SF_6 and CF_3SO_2F are mixed with H_2O to acquire their static reactions. Based on the predicted structures with the lowest total energy based on Monte-Carlo methods in polymorph code, the four structures are further optimized in CASTEP with GGA-PBE method in Fig. 3.

Table 3 Molar absorption coefficient based on infrared spectrum ε, spectrally resolved radiative forcing F_i and σ_i under the level of M062X/def2tzvp

ε	F_i [W m^{-2} cm (cm^2 molecule^{-1})$^{-1}$]	σ_i (cm molecule^{-1})
1525	0.0341	0.015
1319	0.3335	0.015
1303	0.207	0.015
1189	1.52	0.015
869	3.135	0.015
796	2.74	0.015
630	0.6145	0.015
574	2.13	0.015
500	1.67	0.015

The optimized structures with the corresponding DOS maps are shown in Fig. 4. Using the HSE06 hybrid functional, we calculated the band gaps of the electronic structures for SF_6 and SF_6–H_2O. The crystalline SF_6 adopts $P_{21\text{-}c}$ space group with the band gap of 7.56 eV, where the crystal parameters are $a = 4.59$ Å, $b = 8.69$ Å, $c = 9.12$ Å, $\alpha = 90.0°$, $\beta = 120.9°$, $\gamma = 90.0°$ (Fig. 4a). As the mixed model of the crystalline SF_6–H_2O in Fig. 4b, the band gap is decreased to 4.43 eV compared with SF_6. The crystal parameters are $a = b = 4.65$ Å, $c = 23.42$ Å, $\alpha = 113.63°$, $\beta = 120.9°$, $\gamma = 67.5°$ with the space group of $C_{2\text{-}c}$. The density of states of SF_6 and SF_6–H_2O are compared in Fig. 4c and d. S 3s and 3p states occupy the lowest energy area in both structures. In the area of −5 eV to Fermi level, the most active electron states are contributed from O 2p and H 1 s states. In the structure of SF_6–H_2O, we notice that the occupied energy level of both S 3s/3p and F 2p states is decreased. However, the energy level of O 2p and H 1s states are both centered around Fermi

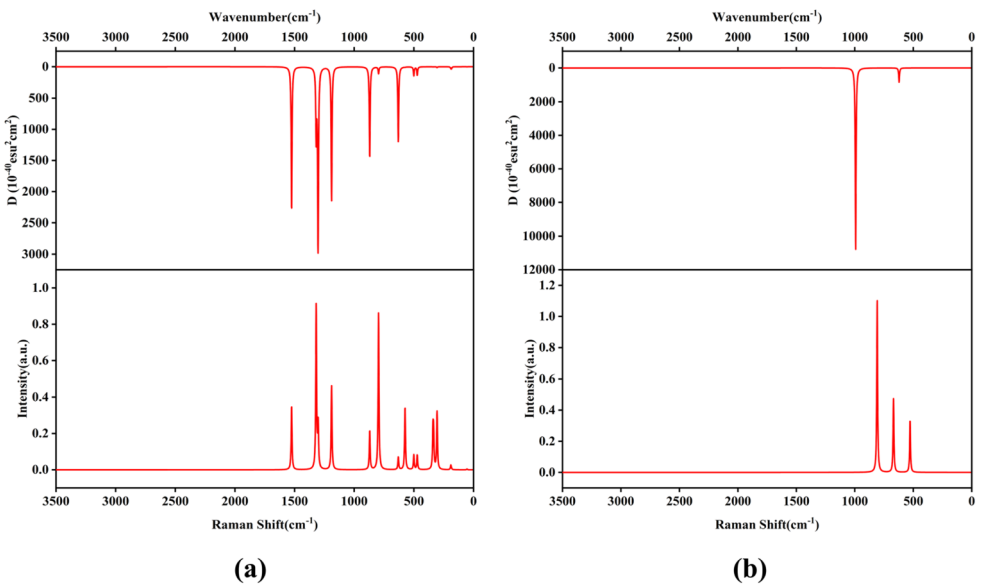

Fig. 2 Infrared spectra (top) and Raman spectra (bottom) of CF_3SO_2F (a) and SF_6 (b).

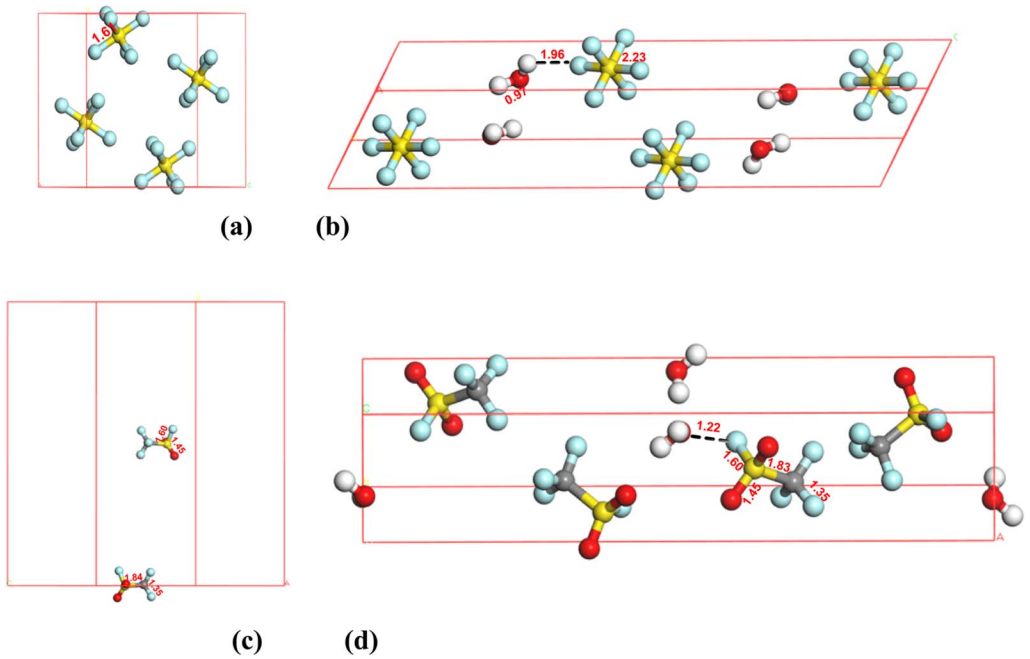

Fig. 3 The two predicted crystal structures. Top left is SF_6(a), Top right is SF_6–H_2O(b), lower left is CF_3SO_2F (c), lower right is CF_3SO_2F–H_2O (d).

level, indicating that the doped H_2O increase the reactivity of SF_6 caused by the highly active O 2p and H 1s electronic states.

As for CF_3SO_2F, corresponding band gaps were obtained through independent HSE06 calculations of the electronic structures; the predicted crystal CF_3SO_2F adopts P_{21} space group with the band gap of 6.56 eV. The crystal parameters are $a = 15.39$ Å, $b = 25.92$ Å, $c = 18.54$ Å, $\alpha = 90.0°$, $\beta = 100.61°$, $\gamma = 90°$ (Fig. 5a), where the most active electron states are composed of C 2p, F 2p and O 2p states closed to the Fermi level of DOS map in Fig. 5b. Crystal CF_3SO_2F–H_2O adopts P_1 space group with the band gap of 2.47 eV and the crystal parameters of $a = 4.59$ Å, $b = 8.69$ Å, $c = 9.12$ Å, $\alpha = 90.0°$, $\beta = 120.9°$, $\gamma = 90.0°$ (Fig. 5c). Based on the DOS map in Fig. 5d, with introducing H_2O, the high active O 2p and H 1s electronic states occupy the area closed to the Fermi level. Compared with Fig. 5c, the energy level of F 2p, S 3p, and C 2p states of CF_3SO_2F are decreased to overlap with the occupied energy area of O 2p and H 1s states, indicating that the doped ·OH groups (molecular water) increase the reactivity of CF_3SO_2F with forming CF_3SO_2F–H_2O interaction. Moreover, compared with SF_6–H_2O, more kinds of active electronic states around Fermi level indicate the possible high reactivity of CF_3SO_2F–H_2O, which is the determining factor for the dissociation of insulation gases in air.

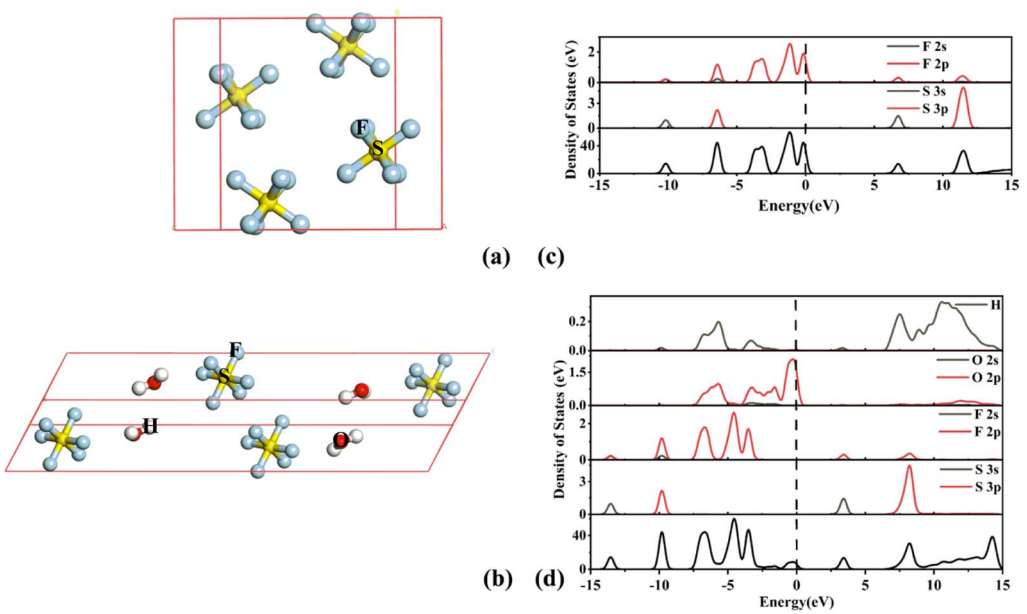

Fig. 4 The predicted crystal SF_6 (a) and SF_6–H_2O (b), and the corresponding DOS maps for SF_6 (c) and SF_6–H_2O (d).

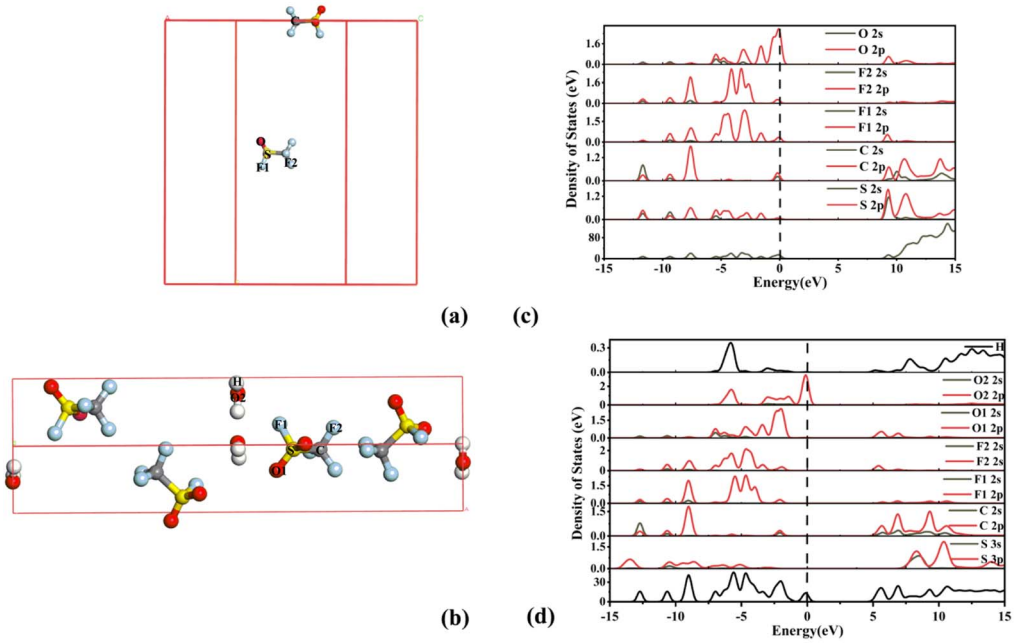

Fig. 5 The predicted crystal CF_3SO_2F (a) and CF_3SO_2F–H_2O (b), and the corresponding DOS maps for CF_3SO_2F (c) and CF_3SO_2F–H_2O (d).

Based on the optimized solid-state crystal structures, we analyzed the electron distribution by comparing the charge density difference shown in Fig. 6, where the green part represents the electron-rich area and the red part is the electron-deficient area. The charge density difference plot reveals electron redistribution between atoms during chemical bond formation. The charge density difference ($\Delta\rho = \rho_{(AB)} - \rho_{(A)} - \rho_{(B)}$) quantifies electron redistribution during chemical bonding, visualized through isosurface plots that reveal regions of electron accumulation ($\Delta\rho > 0$) and depletion ($\Delta\rho < 0$).[51] Without introducing H_2O, electrons in SF_6 are primarily distributed on the surface of F atoms, with charge transferring from S to F. In CF_3SO_2F, the S=O bonds exhibit the highest polarizability and appear to have the strongest electron-withdrawing effect, resulting in a polarized structure with charge transfer from the C–F bond to the S=O bonds. With the introduction of H_2O, charge from F atoms in SF_6 and O atom in CF_3SO_2F transfers to H, forming hydrogen bonds (F···H–O and O···H–O, respectively). This is consistent with the results from DOS analysis, which indicates that H_2O enhances the reactivity of insulation gas due to the high active O 2p and H 1s electronic states, leading to the continuous dissociation. Furthermore, the stronger interaction between the insulation gas and water facilitates dissociation in atmospheric environments. To quantify this, we compare the interaction between water and the insulation gases using the reaction: $SF_6/CF_3SO_2F + H_2O \rightarrow SF_6$–$H_2O/CF_3SO_2F$–$H_2O$. For SF_6–H_2O, the interaction strength between SF_6 and H_2O is 0.22 eV, which is lower than that of CF_3SO_2F–H_2O (0.25 eV), indicating the competitive structure of S–F···H–OH is easier to form for CF_3SO_2F in the atmosphere.

3.4 Atmospheric behaviours of CF_3SO_2F based on CPMD simulation

To understand the dissociation of CF_3SO_2F in atmospheric environments, we employed CPMD to simulate the dynamic pathways between CF_3SO_2F and ·OH, the latter being generated from H_2O in the simulation.[33] We first determined the decomposition pathways of pure CF_3SO_2F in Scheme 1. For comparison, decomposition pathways of pure SF_6 in Scheme S1. To accelerate the decomposition, we set the temperature to 3000 K in equilibrium systems to observe the trajectories. This

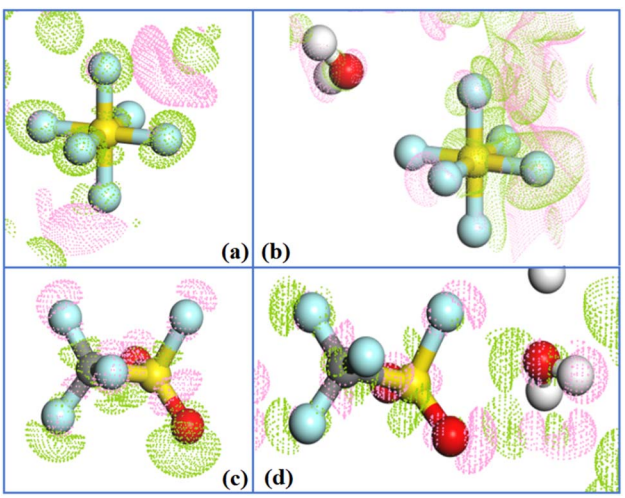

Fig. 6 The charge density difference of SF_6 (a) and SF_6–H_2O (b); CF_3SO_2F (c)and CF_3SO_2F–H_2O (d) in the crystal; Green part represents the electron-rich area; red part is the electron-deficient area, where the iso value of the surface has been set as 0.001 e per $Bohr^3$.

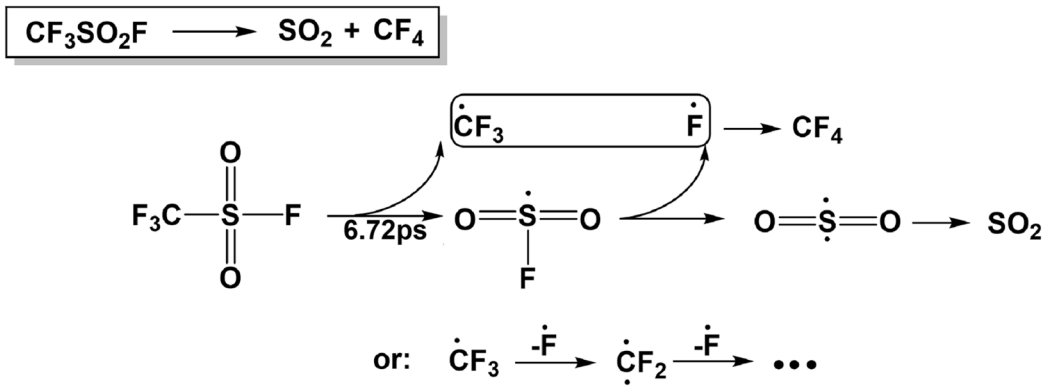

Scheme 1 The summarized decomposition reaction (in the box) with the corresponding pathway of pure CF_3SO_2F at 3000 K from the initial decomposition of 6.72 ps.

approach is also motivated by the fact that protective gases in high-voltage insulation equipment undergo arc discharge, where central temperatures can reach 5000 to 30 000 K.[52,53] Using elevated temperatures thus helps elucidate dissociation mechanisms under these extreme conditions and continuous atmospheric decomposition pathways. In the case of CF_3SO_2F, no cleavage of the S=O bonds was observed. Instead, $CF_3\cdot$ and fluorine radicals dissociated sequentially *via* breaking of the S–C bonds, consistent with the BDE results in Fig. 1, which identify the S–C bond as the weakest in CF_3SO_2F. At ultrahigh temperatures, the generated active radicals can recombine, potentially forming products such as SO_2 or CF_4, as outlined in Scheme 1.

Given that the primary process for the removal of greenhouse gases involves their reaction with tropospheric ·OH,[50] the reaction between CF_3SO_2F and ·OH were analyzed *via* four distinct pathways based on the results of CPMD, denoted as path (a) to path (d) in Scheme 2. It was reported that the precision of energy and rate constants can be achieved to one decimal place.[54] Therefore, the calculated energies and reaction rate constants are rounded to one significant figure. The atomic coordinates of the transition state structure are presented in Table S7. And the reaction energy barrier was comput ed as the difference between the transition state and reactant energies, while the Gibbs free energy change (ΔG_m) was derived from the energy difference between products and reactants, which is in Table 4. These pathways are consistent with previously reported results from designed reactions.[55,56] Path (a) is a nucleophilic substitution reaction in which ·OH, acting as a highly reactive electrophilic reagent, attacks the central sulfur atom. The transition state (TS-a) is reached at 10.12 ps, leading to the formation of $HOSO_2F$ and $CF_3\cdot$. This pathway crosses an energy barrier of 49.5 kcal mol^{-1} and releases 25.1 kcal mol^{-1} of energy. In Path (b), ·OH attacks the electron-deficient carbon atom in the CF_3SO_2F molecule, resulting in cleavage of the S–C bond *via* transition state (TS-b) at 15.78 ps. This step produces CF_3OH and $\cdot SO_2F$, with an energy barrier of 106.7 kcal mol^{-1} and a Gibbs free energy change (ΔG) of 43.9 kcal mol^{-1}. In paths (c) and (d), F· are generated, but the attack sites of the ·OH are different. Although paths (c) and (d) both generate F·, their mechanisms differ in the site where the ·OH attacks. In path (c), the reaction proceeds through transition state (TS-c) at 16.53 ps, yielding CF_3SO_2OH and F·. The energy barrier is 37.6 kcal mol^{-1}, and the Gibbs free energy of reaction is 13.2 kcal mol^{-1}. Path (d) proceeds through transition state (TS-d) at 18.67 ps, forming CF_2OHSO_2F and F·, with an energy barrier of 69.0 kcal mol^{-1} and Gibbs free energy of reaction of 16.3 kcal mol^{-1}. For comparison, the reaction between SF_6 and ·OH were analyzed in Scheme S2, and the Gibbs free energy change was showed in Table S8.

In the four pathways, the most possible dissociation pathway is path (c), triggered by the bond splitting of the weakest SO_2–F bond. The corresponding energy barrier of TS-(c) is the lowest of the four. In the atmosphere, the lifetime of CF_3SO_2F is dominated by the rate-determining step in the interaction with ·OH, which should be the dissociation path (c) with the lowest energy barrier (37.8 kcal mol^{-1}) of the four, rather than the other paths.

To further assess the applicability of M062X/def2tzvp method, the MP2/def2tzvp theoretical approach was employed to compute Path (c) of the reaction between CF_3SO_2F and ·OH (see Table S9). The relative energy of the products and energy barrier obtained using the MP2/def2tzvp method are 1.6 kcal mol^{-1} and 4.9 kcal mol^{-1} higher than those derived from the M062X/def2tzvp method, respectively. The rate constant ($k_{\cdot OH}$) calculated at the MP2/def2tzvp level of theory is 3.9×10^{-19} mol^{-1} cm^3 s^{-1}, whereas the $k_{\cdot OH}$ value obtained at the M062X/def2tzvp method level is 1.3×10^{-15} mol^{-1} cm^3 s^{-1}. This discrepancy arises from the intrinsic characteristics of the respective theoretical methods and falls within the normal range of computational deviations. Therefore, the results obtained at the M062X/def2tzvp level of theory are reasonable.

In the troposphere, the primary source of ·OH is water vapor,[56] with its concentration significantly lower than that of the latter. Therefore, the reaction between CF_3SO_2F and H_2O also merits consideration. The reaction leading to the formation of CF_3SO_2OH and HF (Scheme S3) exhibits the lowest energy barrier (57.2 kcal mol^{-1}), which is still higher than that of Path (c). Consequently, reaction between CF_3SO_2F and H_2O proceeds sluggishly, consistent with previous experimental and theoretical studies.[57,58] Besides, the reaction rate constant (k_{H_2O}) for the reaction between CF_3SO_2F and H_2O is 6.5×10^{-30} mol^{-1} cm^3 s^{-1},while $k_{\cdot OH}$ for Path (c) is 1.3×10^{-15} mol^{-1} cm^3 s^{-1},

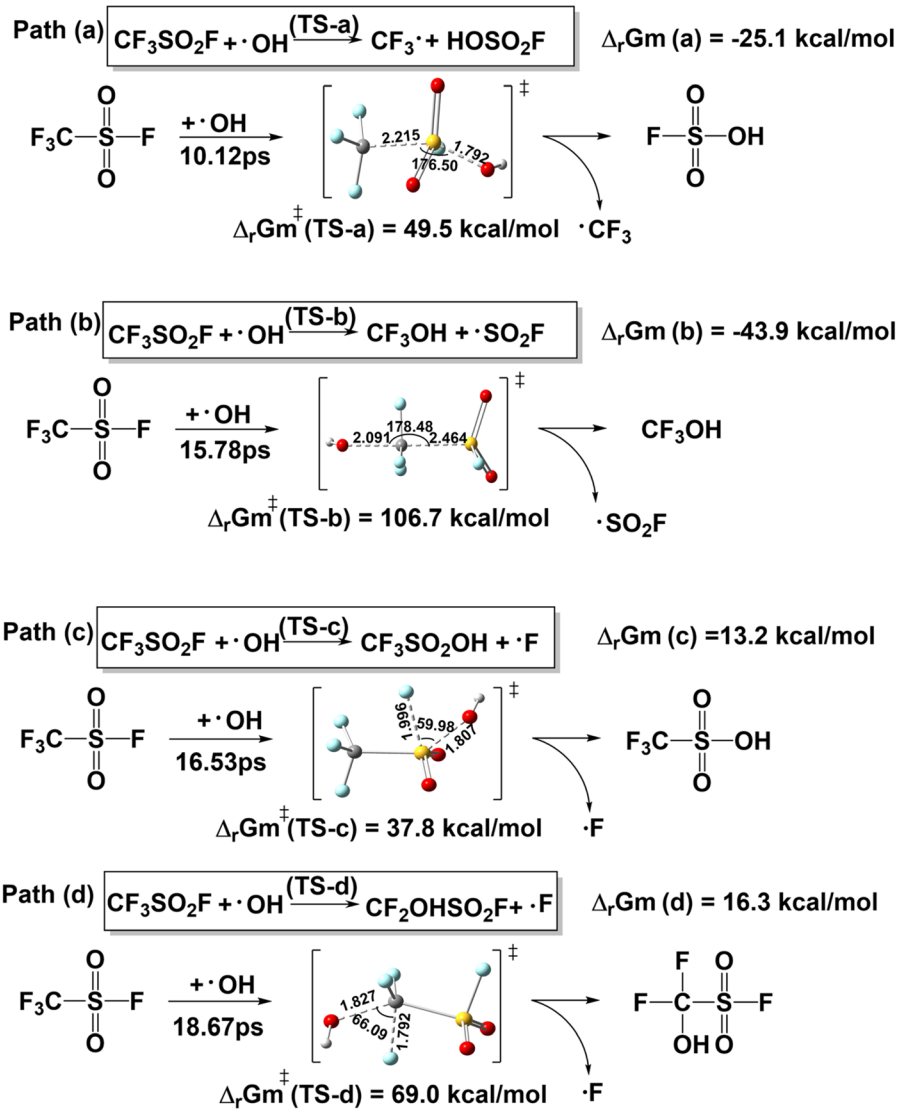

Scheme 2 Four pathways of the interaction between CF_3SO_2F and hydroxyl radical at 3000 K.

Table 4 The reaction Gibbs free energies (Δ_rG_m/kcal mol^{-1}), energy barriers ($\Delta_rG_m^{\neq}$/kcal mol^{-1}), rate constants ($k_{\cdot OH}$/mol^{-1} cm^3 s^{-1}), and lifetime (τ/year) of CF_3SO_2F at 298 K

Pathways	Δ_rG_m	$\Delta_rG_m^{\neq}$	$k_{\cdot OH}$	τ
Path (a)	−25.1	49.5	2.9×10^{-24}	2.28×10^{10}
Path (b)	−43.9	106.7	3.6×10^{-66}	1.87×10^{52}
Path (c)	13.2	37.8	1.3×10^{-15}	52.02
Path (d)	16.3	69.0	1.5×10^{-38}	4.56×10^{24}

suggesting that the high concentration of water cannot compensate for its deficiency in reaction activity. Hence, CF_3SO_2F remains low reactivity toward water.

The lifetime of CF_3SO_2F is 52.02 years, which can be obtained by eqn (2), close to the predicted lifetime of 40 years.[59] As a comparison, the lifetime of SF_6 in Table S8. The theoretical lifetime of SF_6 is 3296 years, which is reasonable with the experimental value of ~3400 years reported in 2017.[60,61] Finally, we have calculated the GWP value based on RE results (0.177 W (m^2 ppbv)$^{-1}$) and lifetime (52.02 years) of CF_3SO_2F based on eqn (3), which is the most important parameter to evaluate the possibility of application of new insulation gas.

The most widely used metric is the GWP with a 100 year time-horizon (hereafter GWP(100)), which is based on the time-integrated RF due to a pulse emission of a unit mass of gas, normalized by the reference gas CO_2, and was introduced in the first assessment report of the Intergovernmental Panel on Climate Change (IPCC).[62] Based on eqn (4),

$$\mathrm{GWP} = \frac{\int_0^T \mathrm{RE}\left(1 - e^{-\frac{T}{\tau}}\right) dT}{\mathrm{AGWP}} \quad (4)$$

with the $T = 100$ years and AGWP of 1.77×10^{-14} W m^{-2} kg^{-1}.[63] We obtained the GWP of CF_3SO_2F as 4320, which is a reasonable

result to rival the reported value (3678) from IPCC. Combining eqn (4), a GWP value of 22 845 for SF_6, while the IPCC reported GWP value for SF_6 is 23 500. Therefore, the simulation provides a simple and direct method to understand the atmospheric behaviours of insulation gas based on the reasonable trajectories based on DFT method and *Ab initio* molecular dynamics simulation.

3.5 Conclusion

This study provides an effective approach using DFT and CPMD simulations to understand the relationship between the structure and dynamic atmospheric behavior of insulation gases, evaluating CF_3SO_2F as a potential alternative to SF_6. The highly polarized C–F, S–F, and S=O bonds in CF_3SO_2F effectively absorb electrons during arc extinction, while its stronger interaction with ·OH results in faster dissociation and a shorter atmospheric lifetime (50.02 years) compared to that of SF_6 (3296 years). Three dissociation pathways—including synergistic and stepwise mechanisms—were identified, with the rate-determining step involving a synergistic mechanism and an energy barrier of 37.6 kcal mol^{-1}. The GWP of CF_3SO_2F (4320) is significantly lower than that of SF_6 (22 845), indicating that CF_3SO_2F is a promising and environmentally friendly alternative gas for high-voltage equipment. Based on mixed-gas models and systematic trajectory analysis, this approach offers a robust framework for evaluating the atmospheric behavior of candidate insulation gases and extends its applicability to the selection of protective gases in power equipment.

Conflicts of interest

The authors declare no competing financial interest.

Data availability

The data supporting this article have been included as part of the manuscript. For requests about the original data, please do not hesitate to contact the corresponding author.

Supplementary information (SI): structures of molecules and crystals; convergence statements; decomposition pathways; coordinates and parameters of crystals. See DOI: https://doi.org/10.1039/d5ra04357c.

Acknowledgements

The calculations are carried out at the High-Performance Computing Center of Anhui University and Hefei Advanced Computing Center. This work is financed by Anhui Provincial Natural Science Foundation (2208085UD16), the National Natural Science Foundation of China (21701001) and by the Natural Science Research Project of Anhui Province (KJ2020ZD04).

References

1 Z. Cui, Y. Li, S. Xiao, S. Tian, J. Tang, Y. Hao and X. Zhang, Recent progresses, challenges and proposals on SF_6 emission reduction approaches, *Sci. Total Environ.*, 2024, **906**, 167347.
2 H. C. Hodge, W. G. Swalbach and H. Rahn, Toxicity Studies of Sulfur Hexafluoride (SF_6) in Pneumoperitoneum, *J. Am. Pharm. Assoc.*, 1958, **47**, 197–201.
3 P. Billen, B. Maes, M. Larrain and J. Braet, Replacing SF_6 in electrical gas-insulated switchgear: technological alternatives and potential life cycle greenhouse gas savings in an EU-28 perspective, *RSC Adv.*, 2020, **10**, 12345–12356.
4 H. Jiang, C. Xie, Y. Liu, C. Xiao, W. Zhang, H. Li, B. Long, W. Dong, D. G. Truhlar, X. Yang and J. Am, Criegee Intermediates Significantly Reduce Atmospheric $(CF_3)_2CFCN$, *Chem. Soc.*, 2025, **147**, 99.
5 C. Man, J. Wang, K. Gao, Y. Li, Y. Zhang and X. Pei, Detection of Transient Decomposition Products of CF_3SO_2F and C_4F_7N via OES Under Spark and Glow Discharges, *High Volt.*, 2025, 2397–7264.
6 Y. Kieffel, F. Biquez, D. Vigouroux, P. Ponchon, A. Schlernitzauer, R. Magous, G. Cros and J. G. Owens, Characteristics of g^3–an alternative to SF_6, *CIRED*, 2017, **24**, 54–57.
7 A. Beroual and A. Haddad, Recent advances in the quest for a new insulation gas with a low impact on the environment to replace sulfur hexafluoride (SF_6) gas in high-voltage power network applications, *Energies*, 2017, **10**, 1216.
8 Y. Fu, A. Yang, X. Wang, A. B. Murphy, X. Li, D. Liu, Y. Wu and M. Rong, Theoretical study of the neutral decomposition of SF_6 in the presence of H_2O and O_2 in discharges in power equipment, *J. Phys. D Appl. Phys.*, 2016, **49**, 385203.
9 Y. Long, L. Guo, Y. Wang, C. Chen, Y. Chen, F. Li and W. Zhou, Electron swarms parameters in CF_3SO_2F as an alternative gas to SF_6, *Ind. Eng. Chem. Res.*, 2020, **59**, 11355–11358.
10 X. Yu, H. Hou and B. Wang, A priori theoretical model for discovery of environmentally sustainable perfluorinated compounds, *J. Phys. Chem. A*, 2018, **122**(13), 3462–3469.
11 Y. Wang, X. Lin, M. Wang and X. Li, Properties of CF_3SO_2F under the influence of external electric field: A DFT study, *Results Phys.*, 2023, **45**, 106248.
12 Y. Wang, Z. Gao, B. Wang, W. Zhou, P. Yu and Y. Luo, Synthesis and dielectric properties of trifluoromethanesulfonyl fluoride: an alternative gas to SF_6, *Ind. Eng. Chem. Res.*, 2019, **58**, 21913–21920.
13 M. P. Sulbaek Andersen, O. J. Nielsen, B. Karpichev, T. J. Wallington and S. P. Sander, Atmospheric chemistry of isoflurane, desflurane, and sevoflurane: kinetics and mechanisms of reactions with chlorine atoms and OH radicals and global warming potentials, *J. Phys. Chem. A*, 2012, **116**(24), 5806–5820.
14 S. Hu, Y. Wang, W. Zhou, R. Qiu, Y. Luo and B. Wang, Dielectric properties of CF_3SO_2F/N_2 and CF_3SO_2F/CO_2 mixtures as a substitute to SF_6, *Ind. Eng. Chem. Res.*, 2020, **59**, 15796–15804.
15 M. Zhang, H. Hou and B. Wang, Mechanistic and kinetic investigations on decomposition of trifluoromethanesulfonyl

fluoride in the presence of water vapor and electric field, *J. Phys. Chem. A*, 2023, **127**, 671–684.
16 M. K. Vollmer, B. R. Miller, M. Rigby, S. Reimann, J. Kim, T. S. Rhee and R. F. Weiss, Atmospheric histories and global emissions of the anthropogenic hydrofluorocarbons HFC-365mfc, HFC-245fa, HFC-227ea, and HFC-236fa, *J. Geophys. Res.*, 2011, **116**, 2156–2202.
17 A. Beroual, U. Khaled and M.-L. Coulibaly, *Experimental Investigation of the Breakdown Voltage of CO_2, N_2, and SF_6 Gases, and CO_2–SF_6 and N_2–SF_6 Mixtures under Different Voltage Waveforms 11*, 2018, p. 902.
18 S. Papasavva, D. J. Luecken, R. L. Waterland, K. N. Taddonio and S. O. Andersen, Estimated 2017 refrigerant emissions of 2, 3, 3, 3-tetrafluoropropene (HFC-1234yf) in the United States resulting from automobile air conditioning, *Environ. Sci. Technol.*, 2009, **43**, 9252–9259.
19 C. Wang, F. Xie, X. Liu, P. Zhang and X. Wang, Adsorption and gas sensing properties of Cr and Mo modified TaS_2 for CF_3SO_2F decomposition products, *Comput. Theor. Chem.*, 2024, **1240**, 114838.
20 Y. Zhao and D. G. Truhlar, The M06 suite of density functionals for main group thermochemistry, thermochemical kinetics, noncovalent interactions, excited states, and transition elements: two new functionals and systematic testing of four M06-class functionals and 12 other functionals, *Theor. Chem. Acc.*, 2008, **120**, 215–241.
21 F. Weigend and R. Ahlrichs, Balanced basis sets of split valence, triple zeta valence and quadruple zeta valence quality for H to Rn: Design and assessment of accuracy, *Phys. Chem. Chem. Phys.*, 2005, **7**, 3297–3305.
22 M. Frisch, G. Trucks, H. Schlegel, G. Scuseria, M. Robb, J. Cheeseman, G. Scalmani, V. Barone, G. Petersson and H. Nakatsuji, *Gaussian 16*, Gaussian Inc., Wallingford, CT, 2016, vol. 1, p. 572.
23 K. B. Wiberg, Application of the pople-santry-segal CNDO method to the cyclopropylcarbinyl and cyclobutyl cation and to bicyclobutane, *Tetrahedron*, 1968, **24**, 1083–1096.
24 R. L. C. Akkermans, N. A. Spenley and S. H. Robertson, Monte Carlo methods in Materials Studio, *Mol. Simul.*, 2013, **39**, 14–15.
25 T. Lu and F. Chen, Multiwfn: A multifunctional wavefunction analyzer, *J. Comput. Chem.*, 2012, **33**, 580–592.
26 A. K. Rappé, C. J. Casewit, K. Colwell, W. A. Goddard III and W. M. Skiff, UFF, a full periodic table force field for molecular mechanics and molecular dynamics simulations, *J. Am. Chem. Soc.*, 1992, **114**, 10024–10035.
27 W. A. Trzciński, S. Cudziło and L. Szymańczyk, Studies of detonation characteristics of aluminum enriched rdx compositions, *Propellants, Explos., Pyrotech.*, 2007, **32**, 392–400.
28 P. Zorkii, A. Razumaeva and V. Belsky, The Systematization of Molecular Crystal Structures, *Acta Crystallogr. A*, 1977, **33**, 1001–1004.
29 M. Segall, P. J. Lindan, M. Probert, C. J. Pickard, P. J. Hasnip, S. Clark and M. Payne, First-principles simulation: ideas, illustrations and the CASTEP code, *J. Phys. Condens. Matter*, 2002, **14**, 2717.
30 S. Grimme, J. Antony, S. Ehrlich and H. Krieg, A consistent and accurate ab initio parametrization of density functional dispersion correction (DFT-D) for the 94 elements H-Pu, *J. Chem. Phys.*, 2010, **132**, 15.
31 R. Car and M. Parrinello, Unified approach for molecular dynamics and density-functional theory, *Phys. Rev. Lett.*, 1985, **55**, 2471.
32 H. J. Monkhorst and J. D. Pack, Special points for Brillouin-zone integrations, *Phys. Rev. B*, 1976, **13**, 5188.
33 S. I. NOSÉ, A molecular dynamics method for simulations in the canonical ensemble, *Mol. Phys.*, 2002, **100**, 191–198.
34 J. Crapse, N. Pappireddi, M. Gupta, S. Y. Shvartsman, E. Wieschaus and M. Wühr, Evaluating the Arrhenius equation for developmental processes, *Mol. Syst. Biol.*, 2021, **17**, e9895.
35 Q. Guo, N. Zhang, T. Uchimarub, L. Chen, H. Quan and J. Mizukado, Kinetics, products, and mechanism for the reaction of E−CF_3CH=CHC_2F_5 with OH radicals in gas phase and atmospheric implications, *Atmos. Environ.*, 2018, **185**, 7–14.
36 V. C. Papadimitriou and J. B. Burkholder, OH radical reaction rate coefficients, infrared spectrum, and global warming potential of $(CF_3)_2CFCH$=CHF (HFO-1438ezy(E)), *J. Phys. Chem. A*, 2016, **120**, 6618–6628.
37 A. E. Heathfield, C. Anastasi, A. McCulloch and F. M. Nicolaisen, Integrated infrared absorption coefficients of several partially fluorinated ether compounds: CF_3OCF_2H, CF_27HOCF_2H, $CH_3OCF_2CF_2H$, CH_3OCF_2CFClH, $CH_3CH_2OCF_2CF_2H$, $CF_3CH_2OCF_2CF_2H$ and CH_2=$CHCH_2OCF_2CF_2H$, *Atmos. Environ.*, 1998, **32**, 2825–2833.
38 A. E. Heathfield, C. Anastasi, P. Pagsberg and A. McCulloch, Atmospheric lifetimes of selected fluorinated ether compounds, *Atmos. Environ.*, 1998, **32**, 711–717.
39 M. Rabie, D. A. Dahl, S. M. A. Donald, M. Reiher and C. M. Franck, Predictors for gases of high electric strength, *IEEE Trans. Dielectr. Electr. Insul.*, 2013, **20**, 856–863.
40 M. Rabie, D. A. Dahl, S. M. A. Donald, M. Reiher and C. M. Franck, Predictors for gases of high electric strength, *IEEE Trans. Dielectr. Electr. Insul.*, 2013, **20**, 856–863.
41 M. Rabie and C. M. Franck, Computational screening of new high-voltage insulation gases with low global warming potential, *IEEE Trans. Dielectr. Electr. Insul.*, 2015, **22**, 296–302.
42 X. Yu, H. Hou and B. Wang, A priori theoretical model for discovery of environmentally sustainable perfluorinated compounds, *J. Phys. Chem. A*, 2018, **122**, 3462–3469.
43 K. P. Shine and G. Myhre, The Spectral Nature of Stratospheric Temperature Adjustment and its Application to Halocarbon Radiative Forcing, *Geophys. Res. Lett.*, 2020, **12**, 1942–2466.
44 K. P. Shine and G. Myhre, The spectral nature of stratospheric temperature adjustment and its application to halocarbon radiative forcing, *J. Adv. Model. Earth Syst.*, 2020, **12**, e2019MS001951.
45 S. Pinnock, M. D. Hurley, K. P. Shine, T. J. Wallington and T. J. Smyth, Radiative forcing of climate by

hydrochlorofluorocarbons and hydrofluorocarbons, *J. Geophys. Res.*, 1995, **100**, 23227–23238.

46 M. H. Jamróz and J. Cz. Dobrowolski, Potential energy distribution (PED) analysis of DFT calculated IR spectra of the most stable Li, Na, and Cu(I) diformate molecules, *J. Mol. Struct.*, 2001, **565–566**, 475–480.

47 R. Pincus, S. A. Buehler, M. Brath, C. Crevoisier, O. Jamil, K. Franklin Evans, J. Manners, R. L. Menzel, E. J. Mlawer, D. Paynter, R. L. Pernak and Y. Tellier, Benchmark calculations of radiative forcing by greenhouse gases, *J. Geophys. Res.: Atmos.*, 2020, **125**, e2020JD033483.

48 Ø. Hodnebrog, M. Etminan, J. Fuglestvedt, G. Marston, G. Myhre, C. Nielsen, K. P. Shine and T. Wallington, Global warming potentials and radiative efficiencies of halocarbons and related compounds: A comprehensive review, *Rev. Geophys.*, 2013, **51**, 300–378.

49 X. Wan, W. Yu, A. Wang, X. Wang, J. Robertson, Z. Zhang and Y. Guo, High-throughput screening of gas sensor materials for decomposition products of eco-friendly insulation medium by machine learning, *ACS Sens.*, 2023, **8**, 2319–2330.

50 P. Price, B. Bottorff, J. Jenkins, W. H. Brune and P. S. Stevens, Re-assessing hydroxyl radical chemistry in the atmosphere: Instrument interferences may explain previous measurement discrepancies, *Commun. Earth Environ.*, 2025, **6**, 325.

51 M. A. A. Ibrahim, N. K. M. Ahmed, A. H. M. Mahmoud, M. A. El-Tayeb, A. M. M. Abdelbacki, S. Khan, M. E. S. Soliman and T. Shoeib, RuC nanosheet as a promising biosensing material for detecting the aromatic amino aciacids: a DFT study, *Nanoscale Adv.*, 2024, **6**, 6398–6407.

52 Q. Gao, X. Wang, H. Sun, A. Yang and C. Niu, Calculation of the decomposition products of $C_5F_{10}O$-Air mixtures from 500 K to 3500 K with a chemical kinetic model, *Plasma Chem. Plasma Process.*, 2024, **44**, 1883–1903.

53 K. Li, H. Javed, G. Zhang and A. T. Plesca, Analysis of air decomposition by-products under four kinds of partial discharge defects, *IEEE Trans. Dielectr. Electr. Insul.*, 2017, **24**(6), 3713–3721.

54 A. Wang, R. Kingsbury, M. McDermott, *et al.*, A framework for quantifying uncertainty in DFT energy corrections, *Sci. Rep.*, 2021, **11**(1), 15496.

55 C. Man, J. Wang, K. Gao, Y. Li, Y. Zhang and X. Pei, Detection of Transient Decomposition Products of CF_3SO_2F and C_4F_7N via OES Under Spark and Glow Discharges, *High Volt.*, 2025, 2397–7264.

56 D. C. Anderson, B. N. Duncan, A. M. Fiore, *et al.*, Spatial and temporal variability of the hydroxyl radical: Understanding the role of large-scale climate features and their influence on OH through its dynamical and photochemical drivers, *Atmos. Chem. Phys. Discuss.*, 2020, **2020**, 1–32.

57 T. Gramstad and R. N. Haszeldine, 33. Perfluoroalkyl derivatives of sulphur. Part IV. Perfluoroalkanesulphonic acids, *J. Chem. Soc.*, 1956, 173–180.

58 M. Zhang, H. Hou and B. Wang, Mechanistic and Kinetic Investigations on Decomposition of Trifluoromethanesulfonyl Fluoride in the Presence of Water Vapor and Electric Field, *J. Phys. Chem. A.*, 2023, **127**, 671–684.

59 Y. Long, L. Guo, Y. Wang, C. Chen, Y. Chen, F. Li and W. Zhou, Electron swarms parameters in CF_3SO_2F as an alternative gas to SF_6, *Ind. Eng. Chem. Res.*, 2020, **59**(24), 11355–11358.

60 M. P. Sulbaek Andersen, M. Kyte, S. T. Andersen, C. J. Nielsen and O. J. Nielsen, Atmospheric Chemistry of $(CF_3)_2CF$–CN: A Replacement Compound for the Most Potent Industrial Greenhouse Gas, SF6, *Environ. Sci. Technol.*, 2017, **51**, 1321–1329.

61 G. Zhao, H. Kim, C. Yang and Y. G. Chung, Leveraging machine learning to predict the atmospheric lifetime and the global warming potential of SF_6 replacement gases, *J. Phys. Chem. A*, 2024, **128**(12), 2399–2408.

62 C. Smith, Z. R. J. Nicholls, K. Armour, W. Collins, P. Forster, M. Meinshausen, M. D. Palmer, M. Watanabe, The Earth's Energy Budget, Climate Feedbacks, and Climate Sensitivity Supplementary Material, in *Climate Change 2021: the Physical Science Basis. Contribution of Working Group I to the Sixth Assessment Report of the Intergovernmental Panel on Climate Change*, 2021.

63 Ø. Hodnebrog, B. Aamaas, J. S. Fuglestvedt, G. Marston, G. Myhre, C. J. Nielsen, M. Sandstad, K. P. Shine and T. J. Wallington, Updated global warming potentials and radiative efficiencies of halocarbons and other weak atmospheric absorbers, *Rev. Geophys.*, 2020, **58**, e2019RG000691.